

Tunneling cracks in arbitrary oriented off-axis lamina

Lars P. Mikkelsen · Simon J. Klitgaard ·
Christian F. Niordson · Bent F. Sørensen

Received: date / Accepted: date

Abstract The steady-state energy release rate for tunneling cracks under mixed mode loading is determined using finite element predictions. The analysed case is a balanced and symmetric laminate layup $[0/\theta/0/-\theta]_s$ where the tunneling crack is located parallel to the fiber direction of the central off-axis oriented layer. It is found that for the steady-state situation, a simple energy balance calculation of the released energy based on normal and tangential crack opening displacements of the crack surfaces of a fully developed crack gives the same value as the average value of a detailed J-integral analysis of the crack-tip, averaged across the thickness of the tunnelling crack. Furthermore, the crack tip mode mixity, averaged across the layer thickness, was found to agree with the phase angle obtained using the energy balance method. Based on this simplified approach, the energy released rate

Lars P. Mikkelsen
DTU Wind Energy
Technical University of Denmark
Frederiksborgvej 399
4000 Roskilde, Denmark
Tel.: +45 21325406
E-mail: lapm@dtu.dk

Simon J. Klitgaard
Technical University of Denmark
Frederiksborgvej 399
4000 Roskilde, Denmark
E-mail: s.just.k@gmail.com

Christian F. Niordson
DTU Mechanical Engineering
Technical University of Denmark
Nils Koppels Allé
2800 Lyngby, Denmark
E-mail: cn@mek.dtu.dk

Bent F. Sørensen
DTU Wind Energy
Technical University of Denmark
Frederiksborgvej 399
4000 Roskilde, Denmark
E-mail: bsqr@dtu.dk

is determined, covering $\theta \in [0; 90]^\circ$ for orthotropic elastic properties ranging from typical low modulus glass fiber reinforced polymers to high modulus carbon fiber reinforced polymers. The predicted results can be used to investigate the influence of the layup angles on static and fatigue tunnel crack evolution in composite materials used in e.g. wind turbine blades.

Keywords Finite element model · fracture toughness · J-integral · Composite materials · Orthotropic materials · Laminate · Mode mixity

1 Introduction

Conventionally used fiber reinforced polymer matrix composites are orthotropic materials with order of magnitude higher stiffness and strength in the fiber direction than in the transverse direction. Therefore, in order to give acceptable mechanical properties transverse to the main load direction, secondary oriented plies are traditionally included between main load carrying laminas. In addition, the manufacturing procedure may as well require the presence of secondary oriented fiber bundles both in order to ease the handling of the non-crimp fabrics and in order to improve the wetting of the fibers. The load carrying laminates in the spar caps of wind turbine blades will typically be based on non-crimp fabrics with 5-10% secondary oriented fibers [19, 9] in addition to a few off-axis layers in between those quasi-unidirectional plies. Loaded quasi-statically or during cyclic loading, tunneling cracks can initiate and grow in those secondary oriented plies or bundles [13, 18, 7]. In some cases, tunneling cracks can penetrate into the load carrying laminas and induce fibre failure which eventually can lead to final failure [6, 21, 8, 10]. In other cases, crack deflection can occur at the interface to the neighbour uni-directional (UD) ply causing the formation of delamination cracks [16]. In any case, understanding, characterizing and controlling the tunneling crack formation and growth is a central element for improving the fatigue resistance for many load-carrying laminates.

A tunnelling crack is assumed to initiate from a flaw in the off-axis ply or from free edges [17]. Once a crack has formed, it will propagate both in the width direction and the thickness direction, towards the interfaces of neighbouring plies. Having reached the interfaces, the subsequent crack propagation occurs only in the transverse direction parallel with the fibre direction. When the tunneling crack tip front is away from the edges, a steady-state situation is attained. It is then possible to calculate the average energy release rate by energy accounting [2, 4]. The approach uses the crack opening displacement profile far behind the crack tip and the stress state far ahead of the crack tip [4]. More precisely, for a tunneling crack of the height $2h$ the steady state energy release rate was obtained as [4]

$$\hat{G}_{ss} = \frac{1}{2h} \int_0^h \sigma_{22}(z) \delta_n(z) dz \quad (1)$$

where $\sigma_{22}(z)$ is the transverse normal stress far ahead of the crack, $\delta_n(z)$ is the crack opening profile far behind the crack tip and where $(\hat{})$ denotes terms found from the energy accounting approach. The transverse normal stress can be evaluated for a laminate without any cracks, and may suitably be found based on a finite

element model of the un-cracked laminate, or by classical laminate theory representing a infinite large plate.

For a symmetric laminate subjected to tensile loading, the stresses are constant through the thickness in the un-crack lamina. The stress can be taken outside the integration in equation (1) and the expression for the steady state energy release rate can be written as

$$\hat{G}_{ss} = \frac{1}{2}\sigma_{22}\bar{\delta}_n \text{ with } \bar{\delta}_n = \frac{1}{h} \int_0^h \delta_n(z)dz \quad (2)$$

where $\bar{\delta}_n$ denotes the average value of the normal opening $\delta(z)$.

For a tunneling crack in a 90° ply, the crack tip is subjected to pure Mode I. The crack tip shape will therefore adjust itself so that the local energy release rate is constant along the crack front and equal to the Mode I fracture energy, $G(z) = G_{ss}$.

An analyses of channeling cracks with different crack tip shapes, [11] has shown that the stress state only differ a few lamina thickness, $2h$, away from the crack front. Therefore, the stress state ahead of the crack tip will be independent on the actual shape of the crack tip. Consequently, the calculation of energy release rate by the energy accounting approach does not require accurate modelling of the crack front.

In this paper, we generalize the approach for calculation the steady-state energy release rate of a mode I, 90° tunneling crack [2, 4] to a general off-axis tunneling crack. The static and fatigue crack growth-rate of such an off-axis crack growth will depend on both the crack-tip energy release rate $G_{ss}(z)$ and the mode-mixity parameter $\psi(z)$ [5, 12]. In the present work, this will be addressed introducing a through the thickness averaged steady state energy release rate \bar{G}_{ss} and a through the thickness averaged mode mixity parameter $\bar{\psi}$. In the paper, all terms denoted by $(\bar{})$ will indicate an averaged term found using the expression

$$(\bar{}) = \frac{1}{h} \int_0^h () dz, \quad (3)$$

which in the present work will be calculated numerically using the trapezoid rule.

The averaged energy release rate and mode mixity parameters can be calculated from either a crack-tip finite element simulations or by a generalization of the energy approach, Eqs. (1)-(2). It will be shown that the benefit of using the energy approach is that it is not necessary to include the actual crack-tip in the simulation. Following the approach [2, 4], the validation of using the energy change $(\hat{})$ required to form the steady stated crack opening behind the crack tip, $\bar{G}_{ss} \approx \hat{G}_{ss}$ and $\bar{\psi} \approx \hat{\psi}$, will be addressed.

Using the energy accounting approach, the steady state energy release mode, \hat{G}_{ss} , and the mode-mixity, $\hat{\psi}$ for the full off-axis range, $\theta \in]0; 90]^\circ$, will be determined for parameters covering conventional glass, and carbon fiber reinforced polymer composites. Based on those results, experimental works, see e.g. [12, 3] studying the tunneling crack growth rate in different directions can be addressed. Thereby, it will be possible e.g. to determine the optimal angle delaying the tensile fatigue damage initiation coming from backing bundle tunnel cracking as explored in [7, 20].

2 Problem description

2.1 Laminate with an off-axis tunnelling crack

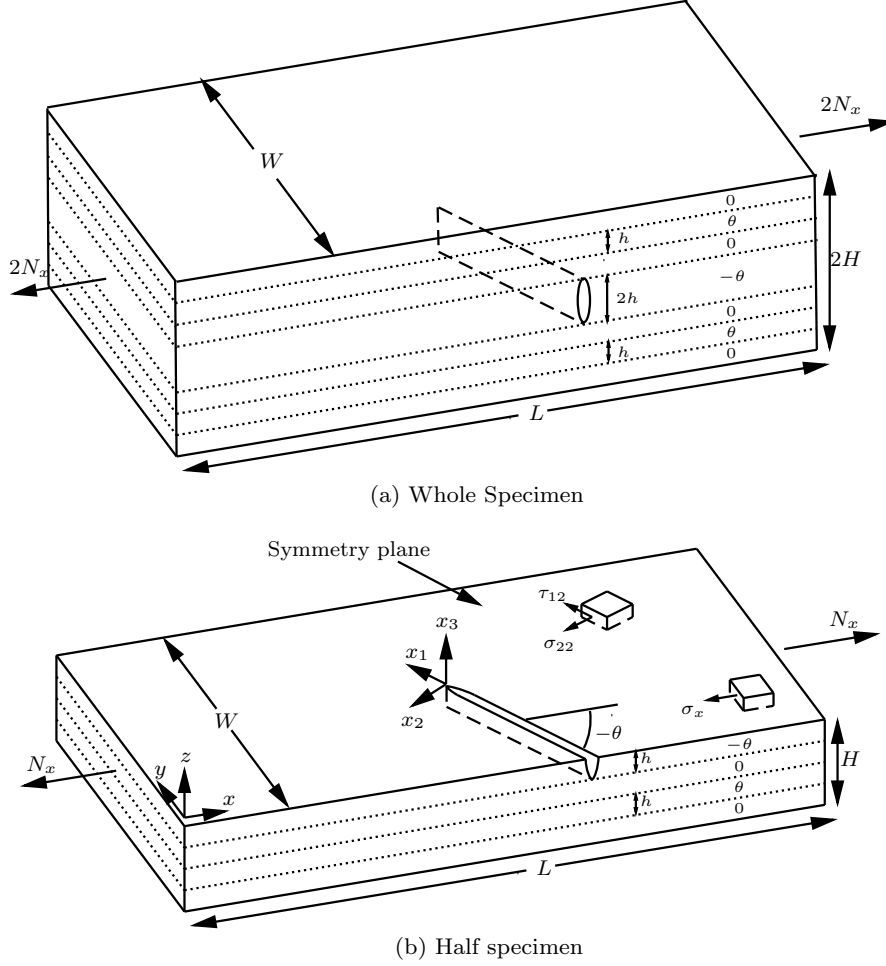


Fig. 1: The plate with the tunneling crack. The global x, y, z coordinate and local coordinate systems x_1, x_2, x_3 are indicated.

The energy release rate for an isolated off-axis tunneling crack is investigated under steady-state growth conditions. The layup investigated is a symmetric and balanced layup $[0/\theta/0/-\theta]_s$ loaded in uniaxial tension as shown in figure 1a. The plate has the overall length L , width W and thickness $2H$. The off-axis crack is located in the central layer of the composite layup in a direction parallel to the fiber direction θ . Since each ply has the thickness h , the off-axis crack has the thickness $2h$. Due to symmetry, only half of the $2H$ thick plate is modelled with

a symmetry boundary condition along the symmetry plane ($z = 0$) as shown in figure 1b. The plate is elongated with a prescribed uniform displacement along the plate end resulting in the axial force N_x .

In the present paper, we operate with two coordinate systems, a global x, y, z coordinate system and a local, ply coordinate system, x_1, x_2, x_3 . In the global coordinate system, x is the loading direction, y is the in-plane width direction, and z is the out-of-plane direction. For the local coordinate system, x_1 is parallel to the fibre direction and x_2 is the in-plane coordinate perpendicular to the fibre direction. The global z and the local x_3 axes coincide and will in the following only be denoted by z .

Table 1: Materials system used

Material unit	E_1 [GPa]	$E_2 = E_3$ [GPa]	$\nu_{12} = \nu_{13}$ [-]	ν_{23} [-]	$G_{12} = G_{13}$ [GPa]	G_{23} [GPa]	λ [-]	ρ [-]
GlassFRP1	30.6	8.62	0.29	0.33	3.25	2.90	0.282	2.34
GlassFRP2	41.2	10.3	0.26	0.41	3.79	3.66	0.250	2.59
CarbonFRP1	126	7.56	0.26	0.40	3.69	2.70	0.060	4.12
CarbonFRP2	266	5.49	0.27	0.40	3.54	2.37	0.021	5.36

The layup is modelled as homogeneous orthotropic materials with material properties covering typical glass and carbon fiber composites. Four material cases are investigated as specified in Table 1. Here, E_1 are the Young's modulus in the fibre direction (the x_1 -direction) while E_2 and E_3 are the Young's modulus in the transverse in-plane, x_2 , and out-of-plane, x_3 , directions, respectively. The in-plane shear modulus is denoted G_{12} , while G_{13} and G_{23} are the out-of-plane shear moduli, respectively. Correspondingly is ν_{12} the major in-plane Poisson's ratio while ν_{13} and ν_{23} the out-of-plane Poisson's ratios. We take the common assumption of transversal isotropy around the fibre direction so that $E_2 = E_3$, $\nu_{12} = \nu_{13}$ and $G_{12} = G_{13}$. The four material systems are denoted GlassFRP1, GlassFRP2, CarbonFRP1 and CarbonFRP2 and correspond to typical composites used in e.g. the wind turbine industry. The properties of the GlassFRP1 is similar to the material investigated in [12]. Together with the material properties, also the two non-dimensional parameters λ and ρ ,

$$\lambda = \frac{E_2}{E_1} \quad \rho = \frac{\sqrt{E_1 E_2}}{2G_{12}} - \sqrt{\nu_{12} \nu_{21}} \quad (4)$$

is calculated. It has been shown [Suo et al., 1991] that for a 2-dimensional orthotropic linear elastic material with prescribed tractions, the stress field depends only on those two parameters and they will be used in the later analysis.

In the following, the results for the stresses, σ , τ , for the crack-openings, δ , for the J-integral and energy release rates, J and G , will be presented in non-dimensional form as follows:

$$\sigma_{22}^* = \frac{\sigma_{22}}{\sigma_x} ; \quad \tau_{12}^* = \frac{\tau_{12}}{\sigma_x} ; \quad \delta^* = \frac{\delta}{2h\varepsilon_x} ; \quad J^* = \frac{J}{2h\varepsilon_x \sigma_x} \text{ and } G^* = \frac{G}{2h\varepsilon_x \sigma_x} \quad (5)$$

Those normalizations have been introduced in order to make the solutions load independent and ply thickness independent where the normalization parameters

ε_x and σ_x is the local axial strain and stress in the off-axis layer obtained from a classical laminate theory while h is the lamina thickness. This normalization factor agrees with the normalization factor $\sigma_x^2 2h / \bar{E}_x$ used by Ho and Suo [4] and by Hutchinson and Suo [5] for the $\theta = 90^\circ$ case. Note that in [4, 5], the normalization parameter contains h instead of as above $2h$ as the total thickness of the tunneling crack in [4, 5] is just h .

3 Theory - tunnelling cracks in orthotropic materials

3.1 Mechanics of cracks in orthotropic materials

For an orthotropic linear elastic material, the relationship between the Mode I and Mode II stress intensity factors, K_I and K_{II} and the Mode I and Mode II energy release rates, G_I and G_{II} , is [Bao et al., 1992]

$$\begin{Bmatrix} G_I \\ G_{II} \end{Bmatrix} = \left(\frac{1 + \rho}{2E_1 E_2} \right)^{1/2} \begin{Bmatrix} \lambda^{-1/4} K_I^2 \\ \lambda^{+1/4} K_{II}^2 \end{Bmatrix} \quad (6)$$

where G_I and G_{II} are the Mode I and Mode II energy release rates.

The linear elastic fracture mechanics mode mixity is defined as the phase angle of the stress intensity factors,

$$\psi = \arctan \left(\frac{K_{II}}{K_I} \right) = \arctan \left(\lambda^{-1/4} \sqrt{\frac{G_{II}}{G_I}} \right). \quad (7)$$

3.2 Analysis of an off-axis tunneling crack

The analysis of the more general case with $\theta \in]0; 90]^\circ$ is described in the following. The stress state at the tunnelling crack front is mixed mode, and the mode mixity ψ may vary as a function of position across the layer thickness, $\psi = \psi(z)$. Since the fracture energy is usually mode mixity dependent, $G_c = G_c(\psi)$ [5], the energy dissipation at the crack front may vary across the thickness of the layer. Still, under steady-state cracking, the crack front will adjust itself so that for all points across the layer, the local energy release rate will be identical to the fracture energy for the associated mode mixity. Consequently, in the steady-state situation, energy dissipation at the crack front will remain the same (independent of crack length) since the crack front retains the same shape and local mode mixity distribution. Both the transverse normal stress σ_{22} and the shear stress τ_{12} will contribute to the energy change. Figure 2 shows the normal $\delta_n(z)$ and tangential $\delta_t(z)$ crack opening displacements of points (e.g. finite element nodes) along the crack.

Consider an advancement Δa of the crack front under steady-state conditions. Although being curved, the crack advance will be the same for all points at the crack tip. The crack front thus maintains its shape and the crack tip moves across the width of the specimen in a self-similar fashion. During steady-state crack growth, the crack tip is remote from edges such that a zone exists far ahead of the crack tip where the stress field is uniform (i.e., independent of x_1 position). Likewise, a zone exists far behind the crack tip in which the crack openings are

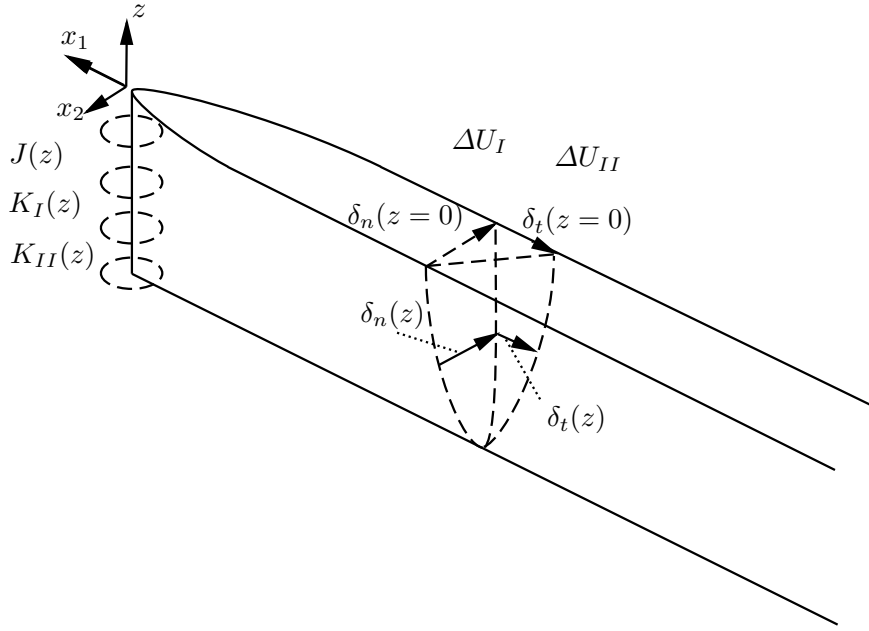


Fig. 2: Sketch of the concept for crack-tip and crack opening analysis,

independent of x_1 position. The stress and displacement fields near the crack tip are invariant, in sense that they translate along with the crack tip in a self-similar manner. For this steady-state situation, a tunnelling crack advance by the distance Δa , corresponds exactly to removing a slice of the laminate of width Δa far ahead of the crack (uniform stress) and inserting a slice of laminate of width Δa far behind the crack tip (uniform crack opening displacements). For fixed applied displacements, the change in the potential energy between the two states (before and after crack advancement) can be determined as the the work required to close the crack and re-establish the stress state as far ahead of the crack:

$$\Delta U = \Delta U_1 + \Delta U_2 \quad (8)$$

where

$$\Delta U_I = \frac{\Delta a}{2} \int_0^h \sigma_{22} \delta_n(z) dz \quad (9)$$

and

$$\Delta U_{II} = \frac{\Delta a}{2} \int_0^h \tau_{12} \delta_t(z) dz. \quad (10)$$

The work for the stresses to close the crack is precisely identical to the reverse problem - the energy released of the advancing crack, or more precisely, the total energy release rate integrated across the layer thickness multiplied by the crack advance Δa ,

$$\Delta U = \Delta a \int_0^h G_{ss}(z) dz. \quad (11)$$

From the expressions (8) and (11) using the expression for the average (3), we can now define an average steady-state energy release rate

$$\hat{G}_{ss} = \frac{\Delta U}{h\Delta a} = \frac{1}{2}\sigma_{22}\bar{\delta}_n + \frac{1}{2}\tau_{12}\bar{\delta}_t, \quad (12)$$

where the two terms in (12) is coming the normal and the tangential opening displacements of the tunneling crack surfaces far behind the crack tip.

In the following, we will split the steady-state energy release rate into two parts, an Mode I part and a Mode II part. Although it cannot be defended rigorously we will base the partitioning of energy release rates on the two terms of the energy accounting method. We well define

$$\hat{G}_I = \frac{1}{2}\sigma_{22}\bar{\delta}_n \quad (13)$$

and

$$\hat{G}_{II} = \frac{1}{2}\tau_{12}\bar{\delta}_t, \quad (14)$$

respectively, so that

$$\hat{G}_{ss} = \hat{G}_I + \hat{G}_{II}. \quad (15)$$

Inspired by equation (7), we can define a nominal mode mixity parameter

$$\hat{\psi} = \arctan\left(\lambda^{-1/4}\sqrt{\frac{\hat{G}_{II}}{\hat{G}_I}}\right). \quad (16)$$

3.3 Finite element models

The tunneling crack problem will be analyzed using finite element models with the discretizations shown in figure 3. In figure 3a, a top-view of the mesh used for J-integral and stress intensity determination is shown. The model represents a plate with the dimension $L \times W = 170h \times 60h$ consisting of around 6 millions 4 noded brick elements with a focused homogeneous mesh at the crack tip with the element dimensions $L_{el} \times W_{el} \times h_{el} = 0.03h \times 0.03h \times 0.008h$. Figure 3b with the dimension of $L \times W = 170h \times 40h$ shows a mesh of around 3.5 millions 4-noded brick elements with a focused homogeneous mesh at the center region of the tunnel-crack with the element dimensions $L_{el} \times W_{el} \times h_{el} = 0.04h \times 0.04h \times 0.01h$ and in Figure 3c the dimensions of $L \times W = 180h \times 220h$ with 5 millions elements again with a focused homogeneous mesh in the center part of the tunnel-crack with the element dimensions $L_{el} \times W_{el} \times h_{el} = 0.04h \times 0.04h \times 0.01h$. The mesh refinement is based on a convergence study ensuring that halving the linear element size results in less than 0.2% change in the calculated energy release rate. In figure 4, a zoomed picture of the focused mesh of the region used for evaluating the J-integral, the stress intensity or the energy change. The solutions from the linear finite element model using Abaqus standard [1] is obtained in 1-4 hours using 200 CPU on a Linux cluster.

Using those meshes, the energy release rate of an off-axis tunneling crack will be analyzed using the following three approaches:

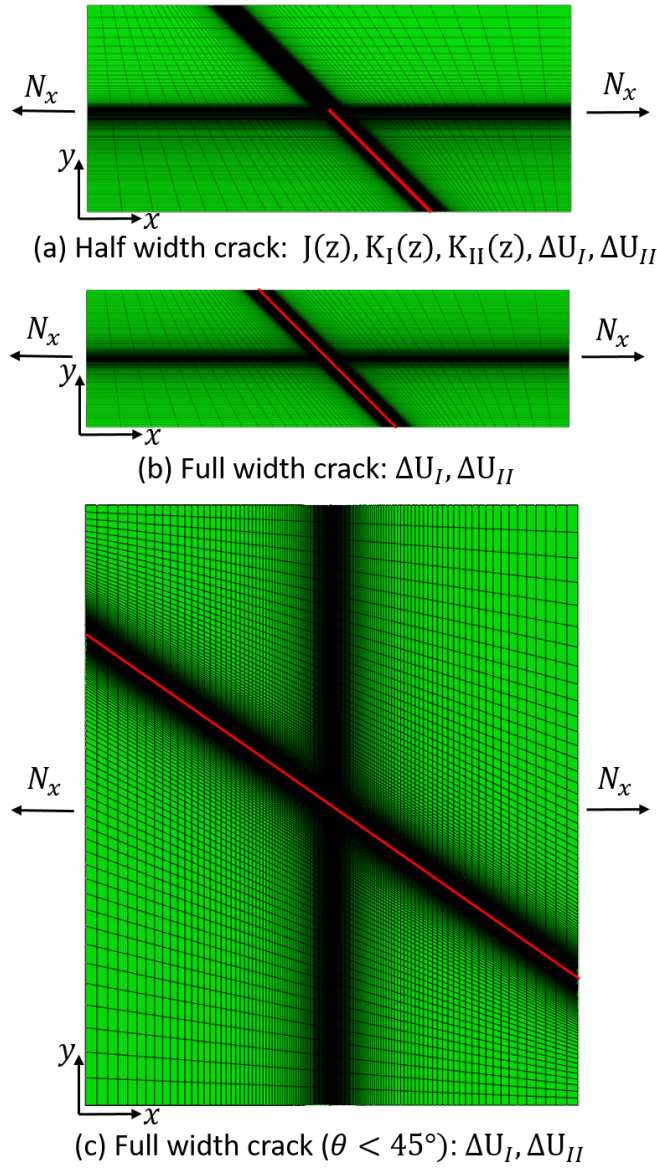


Fig. 3: Top view of finite element mesh where the red line identify the predefined crack.

1. A local J-integral value, $J(z)$, evaluated at points along the straight crack front of the tunneling crack.
2. A local value of the stress intensity factors, $K_I(z); K_{II}(z)$, evaluated along the straight crack front of the tunneling crack.
3. The total energy change, $\Delta U_I; \Delta U_{II}$, calculated from the far-field stress state and the crack opening in a region behind the crack front

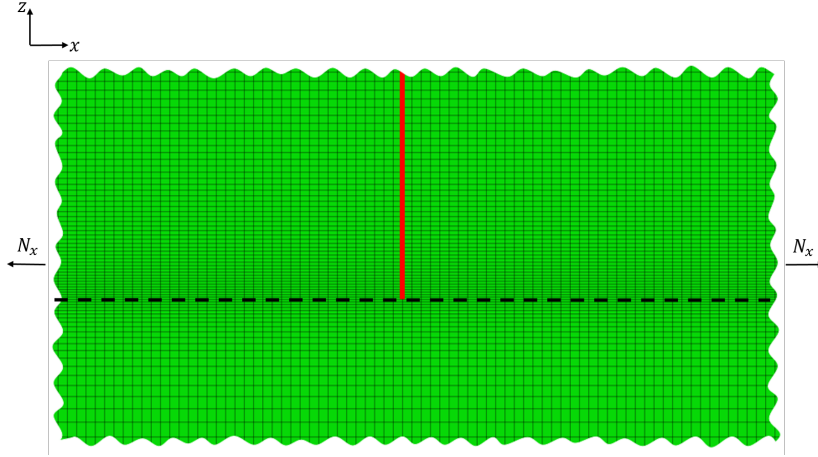


Fig. 4: Zoomed-in side-view of finite element mesh where the red line identify the predefined crack.

Approach 1 utilizes a J-integral evaluation method build in the commercial finite element code Abaqus which are based on a domain integral formulated by [15]. From the J-value along the crack front, a mean J-integral value is calculated as the mean of the mean values for the J-integral for the contours 3-7 around the crack tip, each averaged across the ply thickness, h .

$$\bar{J} = \frac{1}{5} \sum_{k=3}^7 \bar{J}^k \text{ with } \bar{J}^k = \frac{1}{h} \int_0^h J(z) dz \quad (17)$$

where k indicate the contour number.

Approach 2 calculates the local stress intensity factors along the crack front using a build in function in Abaqus. A functionality which can be used to determining the stress intensity factors for an anisotropic material using an interaction integral method as proposed by Shih and Asaro [14]. For more details on the implementation in Abaqus, see [1]. Abaqus can only calculate the stress intensity factors in an homogeneous material, therefore it has been necessary to add a very thin layer of $0.001h$ below the tunneling crack in order to separate the crack-front in the off-axis layer from the 0° layer. Something which only have a negligible effect on the predictions.

Approach 3 is the energy accounting method presented in eq., (12) as a off-axis generalization of transverse tunnel cracking method proposed by Ho and Suo [4]. The method uses the far field stress state calculated using a classical laminate theory and the crack opening profile extracted from the deformed mesh.

The first two approaches require that the FE-model includes the crack-tip as shown for the half-crack in the upper part of figure 5. The third method, the energy accounting approach, does not require a crack-tip in the model. Therefore, the energy accounting calculations can be made by use of the more simple case shown in figure 5. The three approaches are described in more details in the following section.

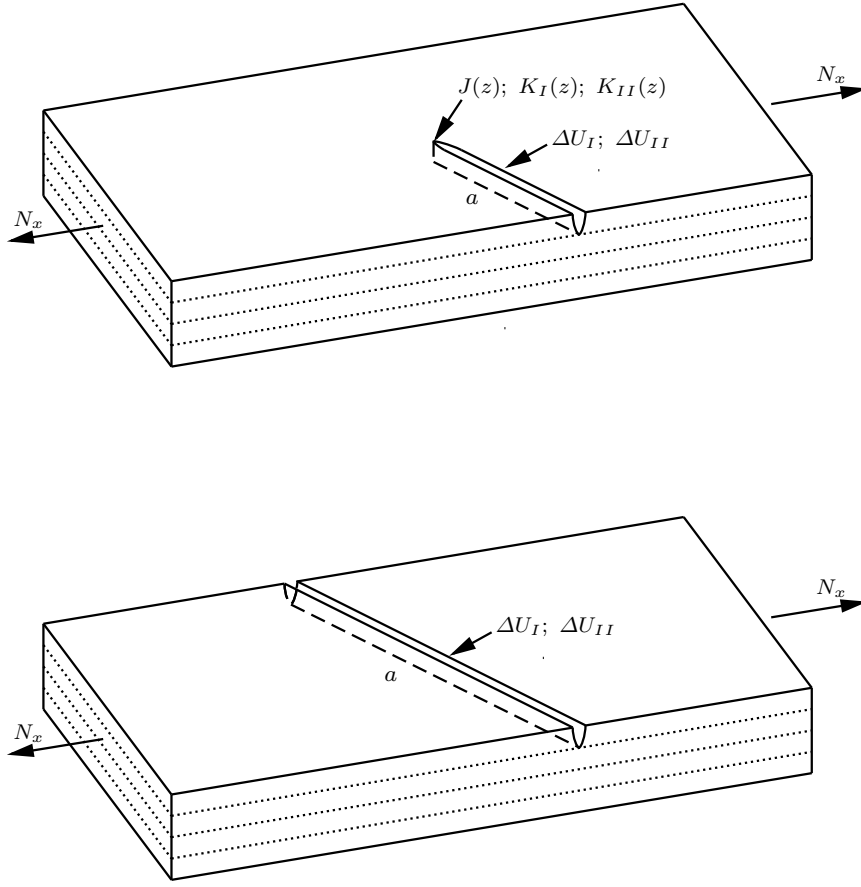


Fig. 5: Determination of the energy release rate for at half-width crack problem (top) and the full-width problem (below)

Results from all three approaches will be compared for the two reference cases GlassFRP1 and CarbonFRP1 with a tunneling crack and off-axis layup given by the angle $\theta = 45^\circ$. A sufficiently large plate geometry is needed in order to obtain converged results, and this is obtained using a plate length on $L/h = 170$ together with a plate width on $W/h = 60$ for the half-width crack case and $W/h = 40$ for the full-width crack case. The problem is judge to be converged when the solutions differ by less than 0.1% when doubling the length or width.

3.4 The energy accounting approach

Figure 6 shows the shear and transverse normal stresses found in the local material coordinate system $(x_1 - x_2)$ in the central off-axis layer for laminate $[0/\theta/0/-\theta]_s$ without a tunneling crack. These stresses will be identical to the stresses ahead of a tunneling crack and are to be used in eq. (12). As expected, a perfect match is

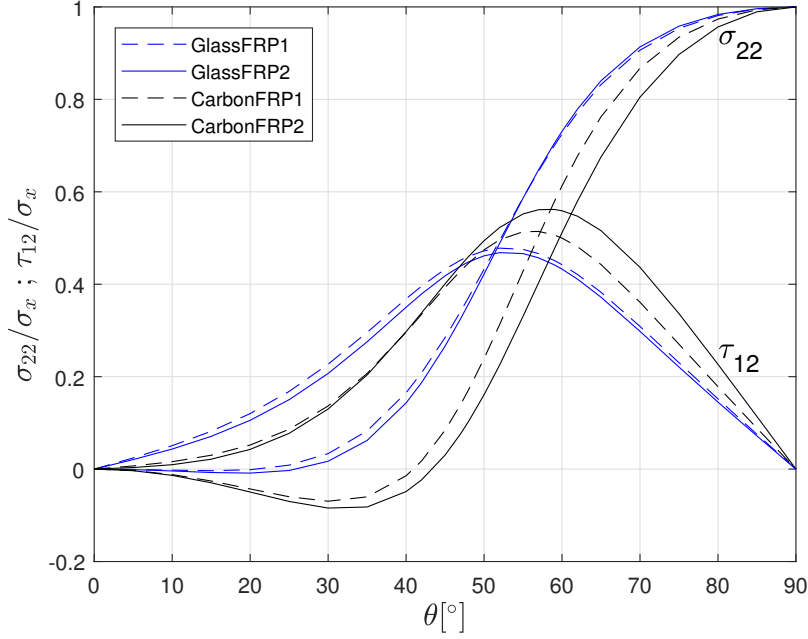


Fig. 6: The normalized stress components σ_{22}/σ_x and τ_{12}/σ_x in the off-axis layer versus the off-axis angle θ found using a classical laminate theory

found between stress components calculated through the classical laminate theory and a linear finite element model of the laminate. In figure 6, the stresses are normalized by the local axial stress σ_x occurring in the off-axis layers. For all four material systems there are compressive transverse normal stresses ($\sigma_{22} < 0$) for small off-axis angles and tensile normal stresses ($\sigma_{22} > 0$) for larger off-axis angles. Hence, for small off-axis angles, a tunneling crack is expected to experience contact between the crack faces and possess compressive normal stresses. For larger angles, the crack-opening normal stress (σ_{22}) is positive and increasing in value until reaching $\sigma_{22}/\sigma_x = 1$ for $\theta = 90^\circ$. The shear stress σ_{12} is always positive and possesses a maximum in the range of $\theta \in [50; 60]^\circ$ depending on the material. As expected for symmetry reasons, σ_{12} vanishes both for $\theta = 0^\circ$ and $\theta = 90^\circ$. Ref [12] studies the two cases $\theta = 50^\circ$ and $\theta = 60^\circ$ for the material GlassFRP1.

In the following, the GlassFRP1 and CarbonFRP1 layup $[0/\theta/0/-\theta]_s$ with $\theta = 45^\circ$ will be used as two reference cases. For those two reference cases with $\theta = 45^\circ$ we have from figure 6 that

$$\begin{aligned} \text{GlassFRP1: } \sigma_{22}^* &= 0.2847, \quad \tau_{12}^* = 0.4327 \\ \text{CarbonFRP1: } \sigma_{22}^* &= 0.0852, \quad \tau_{12}^* = 0.3932 \end{aligned} \quad (18)$$

where the $()^*$ indicate an normalized components following (5). These values will be used below in the calculation of the normalized energy release rate.

Figure 7 show the crack opening displacements of the crack surface far behind the crack tip for the two references cases. Consistent with the results for the normal

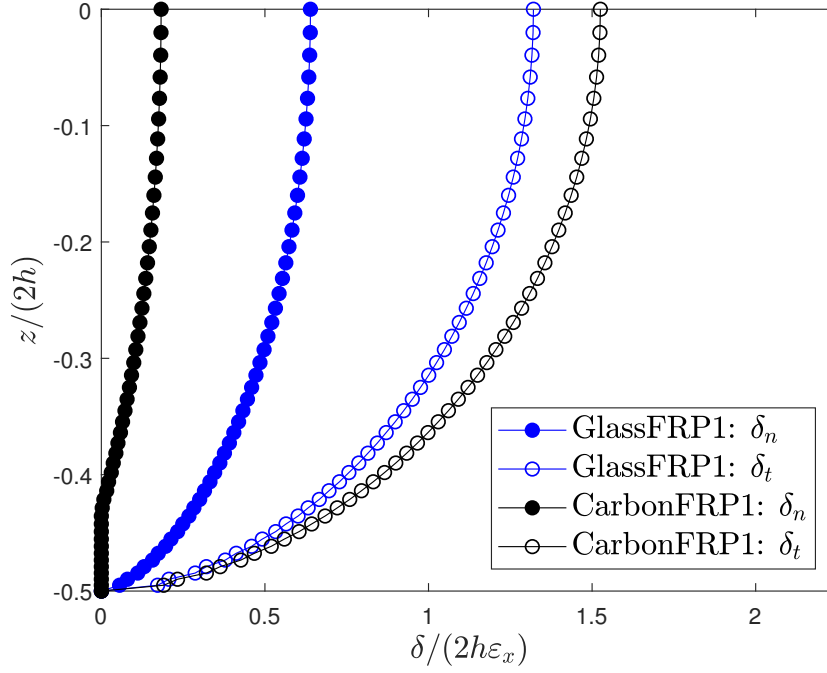


Fig. 7: Normal, δ_n , and tangential, δ_t , crack opening displacements across the layer for the GlassFRP1 and CarbonFRP1 case with $\theta = 45^\circ$

stresses σ_{22} in figure 6, the normal crack opening displacement δ_n is negative for small layup angles. Unlike the negative normal stresses far head of the crack tip, a negative normal opening is physical unrealistic. This model result is an outcome of not taking contact between the crack surfaces into account in the finite element simulations. In the following, those unrealistic negative crack openings will be set equal to zero as shown in the bottom part of the CarbonFRP1 case in figure 7. An average normal and tangential crack opening displacement are - for the two cases shown in figure 7 with $\theta = 45^\circ$ - found to be

$$\begin{aligned} \text{GlassFRP1: } \bar{\delta}_n^* &= 0.4822, \quad \bar{\delta}_t^* = 1.0164 \\ \text{CarbonFRP1: } \bar{\delta}_n^* &= 0.1081, \quad \bar{\delta}_t^* = 1.1696 \end{aligned} \quad (19)$$

Based on equations (12-14), the solid and dotted curves in figure 8 show the average energy release rates, \hat{G}_I , \hat{G}_{II} , and \hat{G}_{ss} calculated using the three approaches for the reference GlassFRP1 case with $\theta = 45^\circ$. A sufficiently large plate has been used with $W = 60h$ for the half crack and $W = 40h$ for the full crack. The length of the plate is $L = 170h$ ($L = 140h$ for J-integral). The curves in figure 8 show the variation of those average energy release rates along the tunnel-crack in the center laminate. The value in the midpoint of the crack ($x_1/a = -0.5$) can - for the GlassFRP1 case with $\theta = 45^\circ$ as shown in figure 8 - be calculated by substituting the earlier obtained values for the GlassFRP1 case shown in equations (18) and

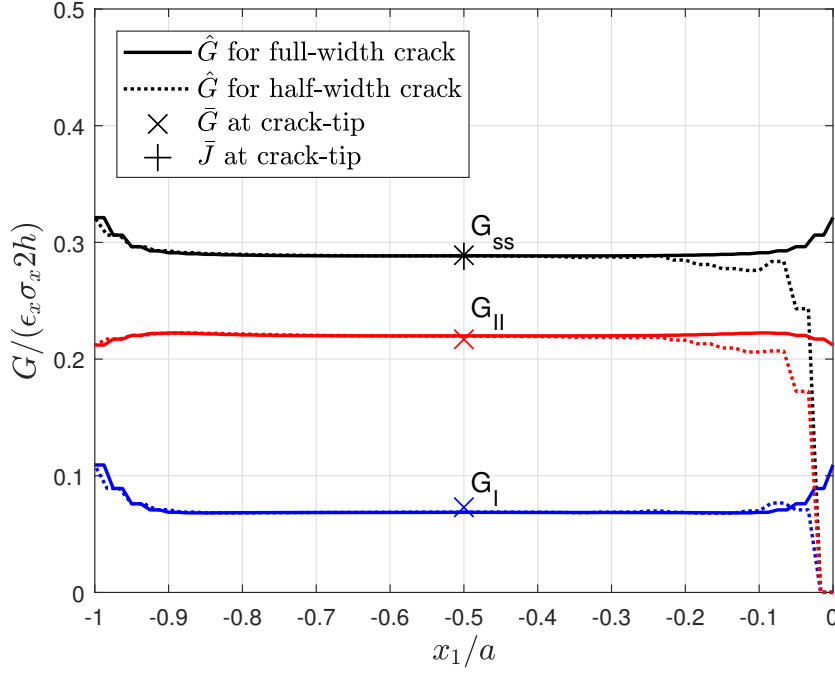


Fig. 8: The variation of the energy change \hat{G}_I and \hat{G}_{II} along the crack analysed for the half-width and full-width crack for GlassFRP1 with $\theta = 45^\circ$. The energy changes is compared with the mean values of the J-integral and energy release rate G calculated from the stress intensity factors as shown in figure 9 and 10. Even though the crack-tip values has been calculated at the crack-tip, $x_1 = 0$, the values has been shown at the crack mid-point, $x_1/a_c = -0.5$, for easing the comparison.

(19) into equations (13) and (14)

$$\hat{G}_I^* = \frac{1}{2} \sigma_{22}^* \bar{\delta}_n^* = \frac{1}{2} \cdot 0.2847 \cdot 0.4822 = 0.0686 \quad (20)$$

$$\hat{G}_{II}^* = \frac{1}{2} \tau_{12}^* \bar{\delta}_t^* = \frac{1}{2} \cdot 0.4327 \cdot 1.0164 = 0.2199 \quad (21)$$

From equations (22) and (16), the energy release rate and the mode mixity parameter is calculated

$$\text{GlassFRP1: } \hat{G}_{ss}^* = 0.289 \text{ and } \hat{\psi} = 67.9^\circ. \quad (22)$$

The corresponding value for the CarbonFRP1 case are

$$\text{CarbonFRP1: } \hat{G}_{ss}^* = 0.235 \text{ and } \hat{\psi} = 86.0^\circ. \quad (23)$$

Figure 8, shows the results obtained along the whole crack path for the two cases shown in figure 5 obtained using the finite element meshes shown in figure 3a and figure 3b. The average energy release rate is calculated along the full-width tunneling crack starting at the laminate edge approaching either the crack tip for case a in figure 3 and 5 or the opposite plate edge for the case b. Except from near

the edge or the crack tip, a rather constant value is found for the average energy release rates confirming the anticipated steady-state nature of the cracking. Those steady-state energy release rate values will, for all the cases analysed in the following, be taken at the midpoint of the crack ($x_1/a = -0.5$).

3.5 Crack-tip simulations

In order to investigate how well those average energy release rate calculated from the energy changes in equations (9-10), represent the actual energy release rates calculated along the crack-tip using the J-integral or stress intensity factor a comparison is made in this sub-section. The average values obtained from those crack-tip simulations are shown in figure 8 as the cross-marks.

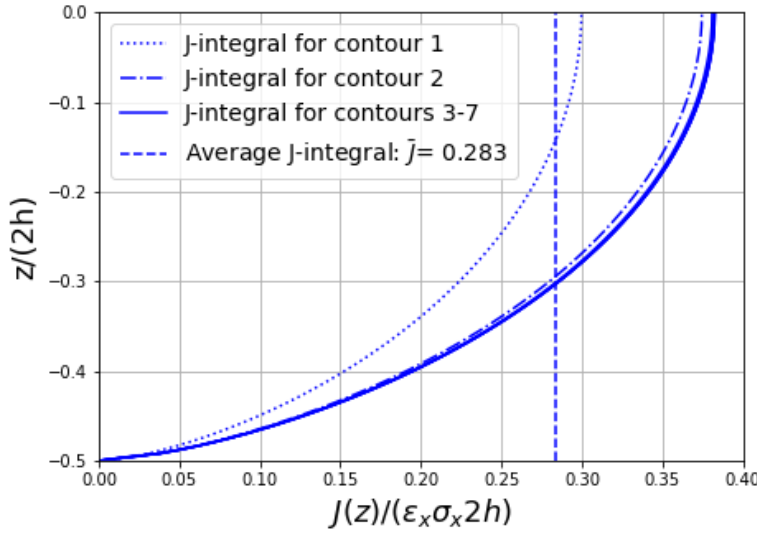


Fig. 9: J-integral along a straight crack front for the GlassFRP1 case with $\theta = 45^\circ$

Figure 9 shows the J-integral evaluated along the tunneling crack tip with a straight crack front orthogonal to the tunneling crack growth direction for the GlassFRP1 case. From Figure 9 it can be seen that except for the first two contours, the J-integral values for the different contours coincide as shown the figure as solid curves lying on the top of each other. This is an expected result; in the steady-state situation, the average value of the J-integral along the any crack front must be identical to the average of the energy release rate obtained by the energy accounting approach, irrespective of the crack tip shape, i.e. also for the case of the straight crack tip. For the GlassFRP1 reference case, the \hat{G}_{ss} obtained in equation (22) is found to differ only 2% from the mean J-integral value found in figure 9.

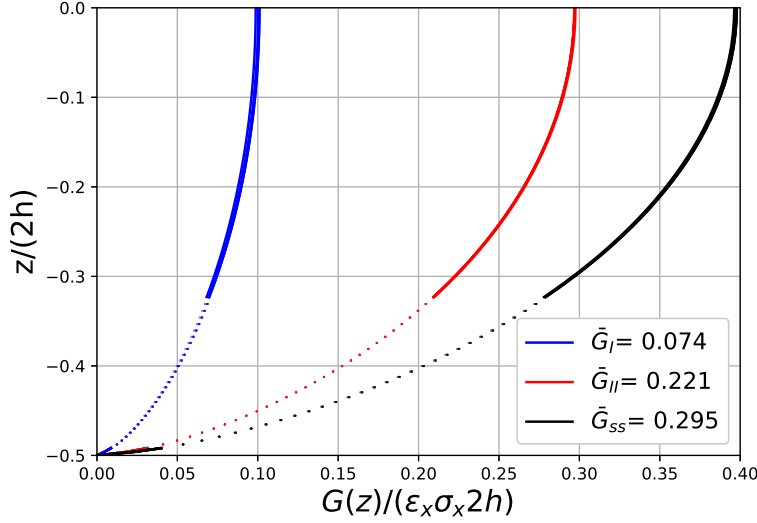


Fig. 10: The local energy release rates, G_I , G_{II} and $G_{ss} = G_I + G_{II}$ along a straight crack front for the GlassFRP1 case with $\theta = 45^\circ$

In addition to the local J-integral, also the stress intensity factors, $K_I(z)$ and $K_{II}(z)$, and thereby the local energy release rates, $G_I(z)$ and $G_{II}(z)$, along the crack front using equations (6) can be determined. Figure 10 show the calculated local energy release rates for the same case with the off-axis direction given by $\theta = 45^\circ$ as used in Figure 9 for the J-integral. It turn out that the build-in method in Abaqus was not able for the specific model to calculate the stress intensity factors (approach 2) along the whole crack front but only in the bottom and upper part of the straight crack. The part in between has been approximated assuming a shape for the energy release rate similar to the J-integral variation across the layer. The approximated part is shown as a dotted line in the figure. In figure 10, the result from the first two contours has been omitted so only the 5 coinciding curves from contours number 3-7 is plotted. The average values (indicated by the dashed line) has been calculated as the average similar to equation (17) for the J-integral. The average energy release rate, $\bar{G}_{ss}^* = \bar{G}_I^* + \bar{G}_{II}^* = 0.295$ differs from the average J-integral value $\bar{J}^* = 0.283$ by 4%. A difference which may come from the missing values in the central part along the crack-front path. The averaged \bar{G}_I , \bar{G}_{II} and \bar{G}_{ss} values was also compared in figure 8 with the values obtained along the crack using the energy change method. Here, a slightly bigger difference was found when comparing \bar{G}_I and \bar{G}_{II} with \hat{G}_I and \hat{G}_{II} than for the comparison of the sums \bar{G}_{ss} , \hat{G}_{ss} and with the J-integral value \bar{J} .

In addition to the local energy release rates, the two local stress intensity factors can also be used to calculate the local mode-mixity along the crack front using the first part of equation (7). For the specific case with a straight crack front the mode-mixity is found to be rather constant along the whole crack front as shown in figure 11.

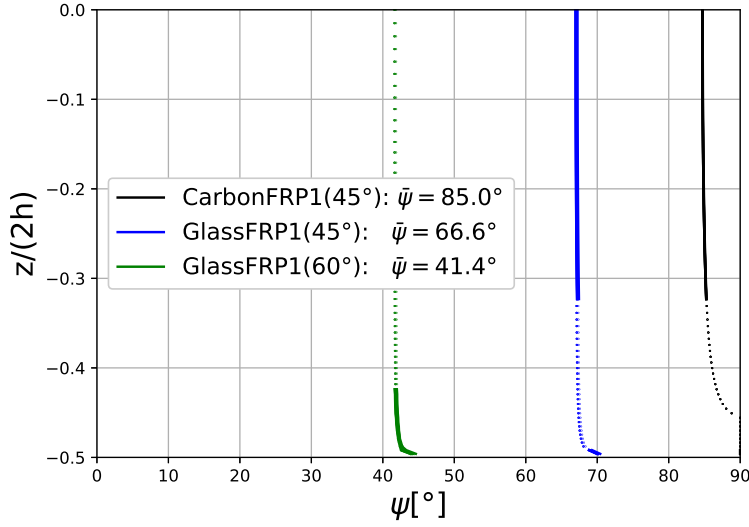


Fig. 11: The local mode mixity along a straight crack front for three cases resulting in three different mode-mixity.

The largest deviation from the average value was found near the bottom of the layer ($z/2h = -0.5$), where the tunneling crack tip stress field is likely to be influenced by the crack tip running along the interface to the neighbour UD layer. For the GlassFRP1 and CarbonFRP1 cases, the average mode mixity parameter based on the crack tip properties, $\bar{\psi}$, was found to be 66.6° and 85.0° , respectively, for $\theta = 45^\circ$. The corresponding mode mixity found using the energy accounting approach was, for the same cases, found to differ only approximately 2% from this.

In summary, by comparing the results obtained from the crack tip and crack opening analysis in the previous section, it was found that there was less than 2% difference for the two cases investigated. Therefore it will in the following be assumed that for all the analysed cases, we can write that

$$\bar{G}_I \approx \hat{G}_I ; \bar{G}_{II} \approx \hat{G}_{II} ; \bar{G}_{ss} \approx \bar{J} \approx \hat{G}_{ss} \text{ and } \bar{\psi} \approx \hat{\psi}. \quad (24)$$

In addition, it was found that the same energy changes was found for the half-width crack and the full-width crack. Therefore, as a conclusion, the mean value of the energy release rate \bar{G}_I , \bar{G}_{II} and \bar{G}_{ss} can be found based on the energy accounting approach found from the full-width crack using the finite element mesh shown in figure 4. A model which do not include the crack tip for which we are predicting the energy release rate for.

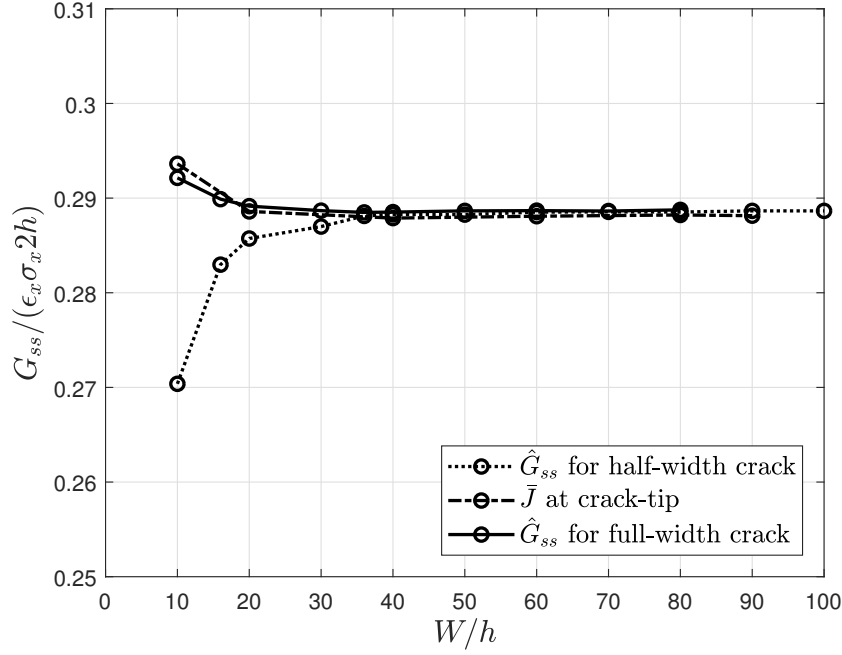


Fig. 12: The convergence of the energy release rate with the plate width W/h for the Glass-FRP1 case with $\theta = 45^\circ$

4 Results

4.1 Effects of plate geometry

Figure 12 show the effect of plate width, W , on the energy release rate for the GlassFRP1 material case with the balanced and symmetric layup $[0/\theta/0/-\theta]_s$ for $\theta = 45^\circ$. For the half-width crack problem, the energy release rate given by the J-integral is highest for small values of W/h decreasing to a converged value for larger values of W/h . A converged energy release rate is obtained for $W = 40h$. It can be seen in figure 12 that all three procedures are converging to the same energy release rate value for larger values of W/h . For smaller W/h , the crack tip "feels" the free edges - there will be no uniform stress field ahead of the crack tip and no uniform crack opening displacements in the crack wake. It is therefore not surprising that \hat{G} obtained by the energy accounting approach is in error for $W/h < 40$ for the half-width problem.

Regarding the plate length, a corresponding convergence has shown that a converge energy release rate value are obtained for $L = 170h$ (or $L = 140h$ for the J-integral), which is the minimum laminate length used in Figure 12.

4.2 Effects of laminate thickness

Figure 13 shows the dependency of the energy release rate on the ratio between the laminate thickness, $2H$, and the lamina thickness, h . In the figure, the laminate

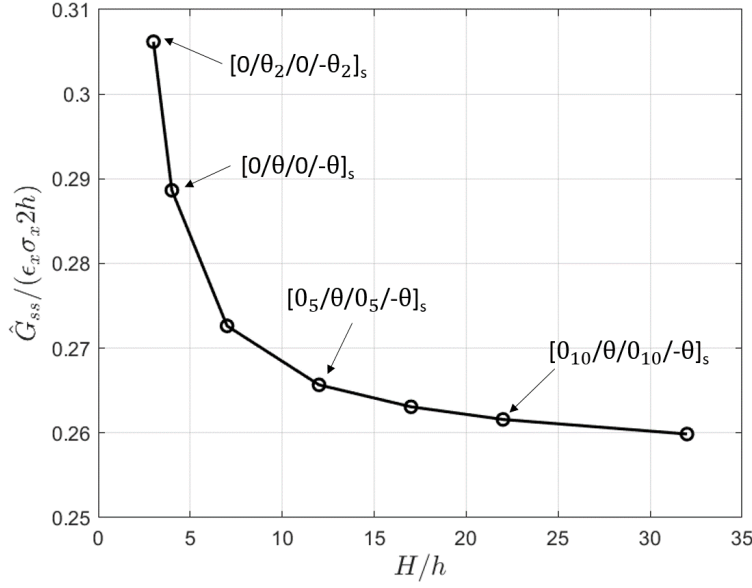


Fig. 13: The dependency of the energy release rate on the ratio between the laminate thickness and the lamina thickness for the GlassFRP1 case with $\theta = 45^\circ$ for a sufficiently large plate with $W = 90h$ and $L = 170h$

thickness is increased by increasing the number of uni-directional (UD) plies next to the tunneling crack, i.e., for laminate lay-ups of the form $[0_n/\theta/0_n/-\theta]_s$, where n is the number of UD plies. It is seen in Figure 13 that the energy release rate decreases with increasing laminate thickness, approaching an asymptotic value for large values of H/h . For the reference case with $[0/\theta/0/-\theta]_s$ ($H/h = 4$), the energy release rate can be seen to be around 15% higher than for the case with an vanishing thickness of the off-axis ply compared with the UD ply. Both the uniform ply thickness case $[0/\theta/0/-\theta]_s$ as well as the large thickness difference is of highly practical relevance. Increasing H/h can also be taken as decreasing h with H fixed, corresponding to a decreasing ply thickness. The later can e.g. represent the tunneling cracking occurring in the off-axis backing layers present in non-crimp fabrics used in the wind turbine industry, where the thickness of the backing bundles is typically significantly smaller than the UD plies, see e.g. [7].

4.3 Effects of crack spacing on the energy release rate

Tunneling cracks in off-axis oriented lamina will occurs as multiple cracking, see e.g. [12, 7]. Therefore, it is important to determined how closely spaced neighboring partly or fully developed cracks can be to a given analysed crack without giving a significant influence on that, i.e., without that the energy release rate and the crack growth behaviour will be influenced. Figure 14 analysis this "critical distance" defined as the closest spacing between an existing full-width crack and a new

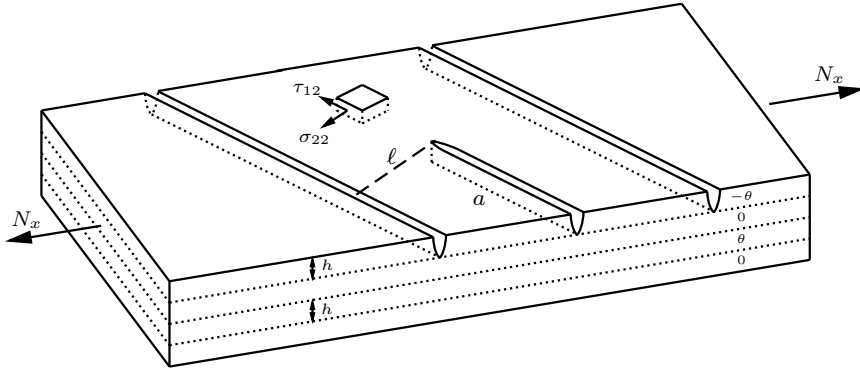
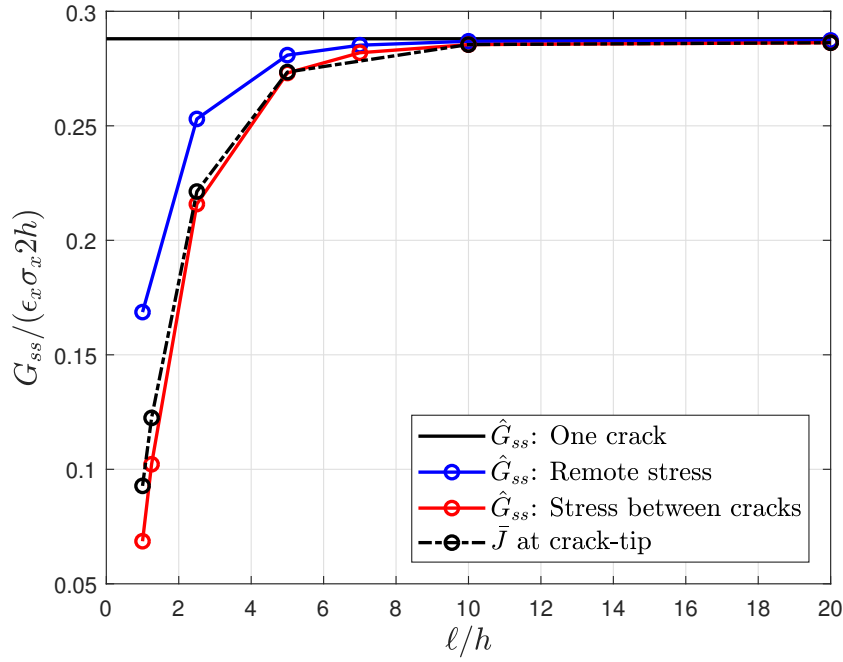


Fig. 14: Sketch of the investigated multiple crack case

propagating tunneling crack for which the energy release rate is identical to that of an isolated tunneling crack.

Fig. 15: Influence of the distance, ℓ , to neighboring cracks on G_{ss} for the GlassFRP1 case with $\theta = 45^\circ$

In the following, this critical distance is determined for the GlassFRP1 case with $\theta = 45^\circ$. Figure 15 shows the energy release rate of the crack tip of a half-width tunneling crack as a function of orthogonal crack spacing, ℓ . The energy

release rate is calculated using both the J-integral and the energy accounting approach. For small ℓ , the steady-state energy release rate is lower than the steady-state energy release rate of an isolated tunneling crack. Compared with \hat{J} and \hat{G}_{ss} for the case without surrounding cracks it has been found that the presence of neighboring cracks lower the energy release rate with less than 1% when the distance is $\ell/h > 10$ to the neighboring crack and with less than 10% when the distance is $\ell/h > 5$. Furthermore, in figure 15 it is found that in order to get a good correlation between the mean value of the J-integral and the energy change \bar{G}_{ss} , the energy change must be calculated based on the stress state between the to surrounding cracks and not as the far-field stress state. ~~Doing this, a good agreement has been found between the mean value of the J-integral along the straight crack front and the energy change calculated behind the crack tip.~~

4.4 Effect of the off-axis crack orientation

Figure 16 show the dependency of \hat{G}_I , \hat{G}_{II} and $\hat{G}_{ss} = \hat{G}_I + \hat{G}_{II}$ with the layup angle θ found for the GlassFRP1 case. The solutions is found for a laminate with a length and a width given to be minimum $W = 40h$ and $L = 170h$. The energy release rate is found from the crack opening profile in the middle of the full-width crack configuration and the layup $[0/\theta/0/-\theta]_s$ is used. For small angles below $\theta < 45^\circ$, the model analysed is modified slightly such that the full-width crack

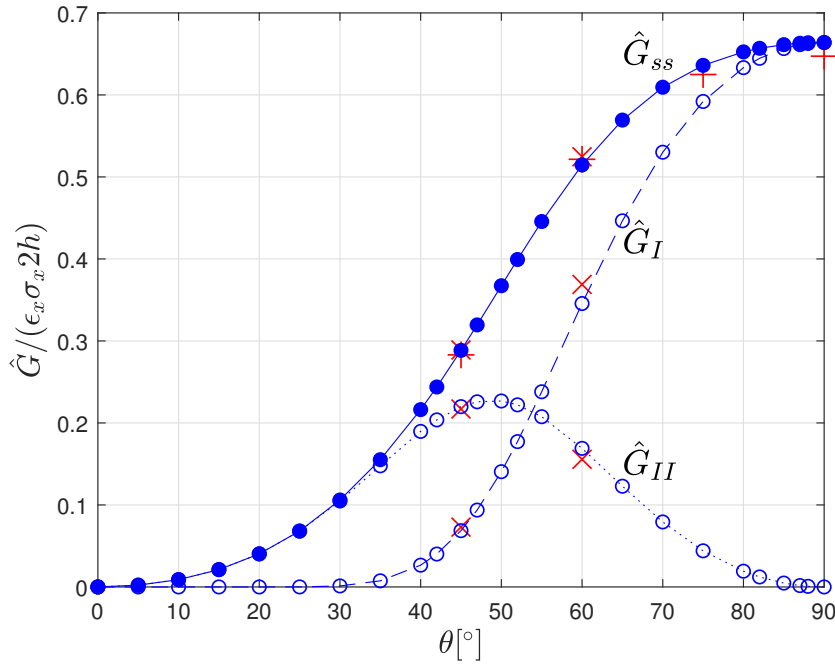


Fig. 16: The energy release rate \hat{G}_I , \hat{G}_{II} and $\hat{G}_{ss} = \hat{G}_I + \hat{G}_{II}$ for the glass fiber composite GlassFRP1. The red markings are the mean G_I , G_{II} , G_{ss} ('x') and J ('+') found along the crack-tip similar to what is done in figure 9 and 10.

ends at the loading ends instead of the sides of the plate. For moderate small angles $\theta \approx 45^\circ$, results from the modified model and the model shown in the lower part of figure 5 was found to coincide.

The shape of the curves in figure 16 for \hat{G}_I and \hat{G}_{II} can be seen to be rather similar with the laminar stress state shown in figure 6. As mentioned earlier, the Mode I energy release rate \hat{G}_I is set equal to zero when no positive normal opening δ_n occur. It is seen in figure 16, that \hat{G}_{ss} increases monotonically with an increasing layup angle θ can be observed where the contribution is going from a purely tangential crack opening displacement, δ_t for $\theta \leq 30^\circ$, to a pure normal opening displacement δ_n for θ approaching 90° . From the red markings on the curves at $\theta = 45^\circ$, it can be seen that there are a good agreement between the energy release rates found from the energy accounting method and the mean value of the crack tip values.

4.5 Effect of the material properties

As an alternative to making a large parametric study on the individual stiffness parameters in the orthotropic material, we investigate the influence of elastic properties on the steady-state energy release rate for the four material cases defined in Table 1. These materials cover the frequently used glass- and carbon fiber based material used in structural application such as in the car, aerospace and wind turbine industry.

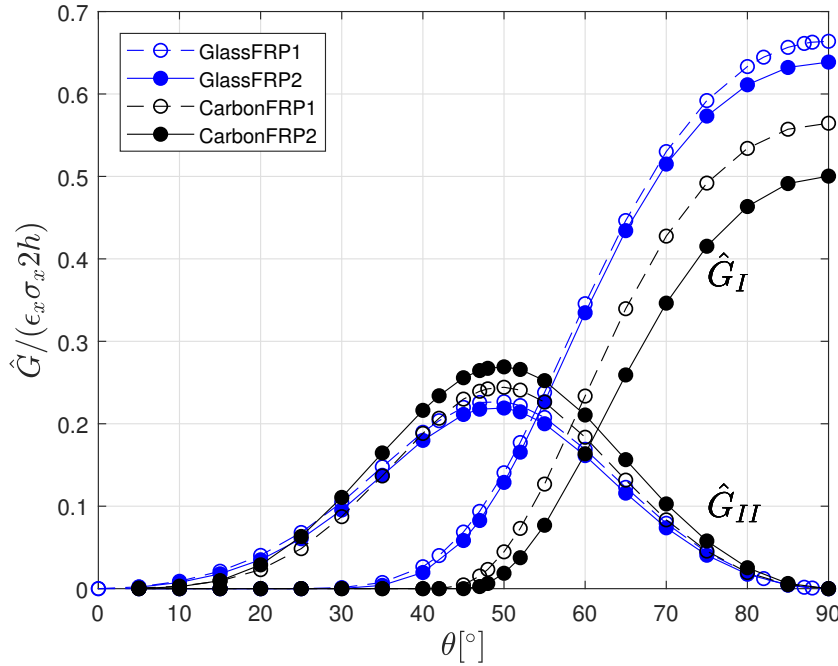


Fig. 17: Energy release rate G_I and G_{II} for all four material cases

In figure 17, \hat{G}_I and \hat{G}_{II} are shown for the four different materials. It can be seen that despite the stiffness properties going from a low modulus glass fiber composite (GlassFRP1) to a high modulus carbon fiber composite (CarbonFRP2), the dependency of the energy release rate to the layup angle θ is rather similar. Nevertheless, it is observed that the higher modulus carbon fiber composite has a lower normalized \hat{G}_I contribution and a slightly higher \hat{G}_{II} contribution than the lower modulus glass fibre composites.

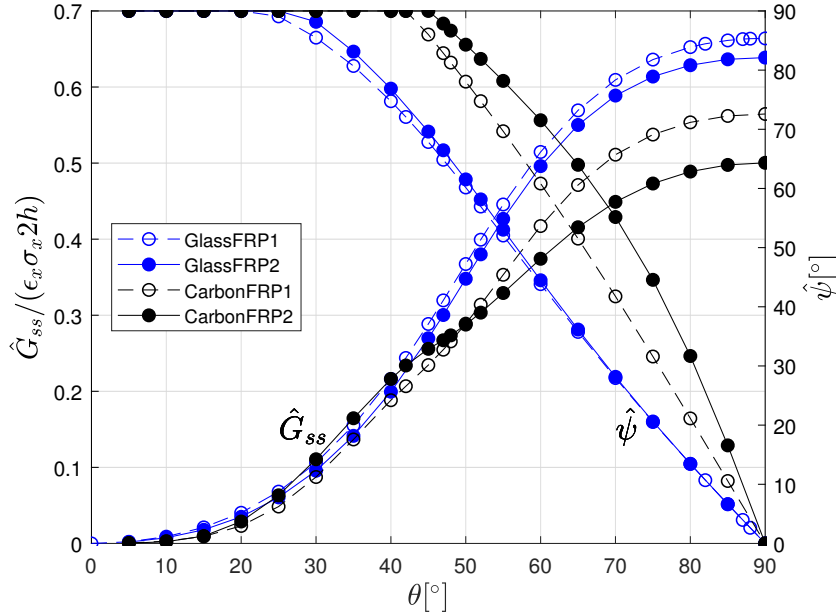


Fig. 18: The total energy release rate \hat{G}_{ss} and mode mixity $\hat{\psi}$ for the 4 material cases

The total energy release rate \hat{G}_{ss} and average mode mixity is shown in figure 18 where the average mode mixity parameter $\hat{\psi}$, defined from (7), is calculated using equation (16). The mode mixity $\hat{\psi}$ is 90° for small values of θ ($\theta < 25^\circ$ for the glass fibre composites; $\theta < 40^\circ$ for the carbon fibre composites), and decreases to 0° for $\theta = 90^\circ$. The dependence of $\hat{\psi}$ on θ is fairly different for the various materials types.

For the glass fibre composites, which have the lowest orthotropy ($\lambda \approx 0.3$; $\rho \approx 2$), experience dominating Mode II ($\hat{\psi} = 90^\circ$) for smaller off-axis angle range ($0 < \theta < 30^\circ$) than the carbon fibre composites ($0 < \theta < 45^\circ$), which have a higher orthotropy ($\lambda \approx 0.05$; $\rho \approx 5$). For larger values of θ , the difference in $\hat{\psi}$ between the two glass fibre composites is very small. In contrast, the results for the carbon fibre composites indicates that increasing orthotropy (decreasing λ , increasing ρ) increases $\hat{\psi}$ for the same θ .

5 Discussion

The energy balance approach proposed by Ho and Suo [4] for a transverse tunnel cracks has been generalized to an analysis of off-axis tunnel cracks. During this, good agreement between the average value of \bar{G}_I , \bar{G}_{II} and \bar{G}_{ss} at the crack tip with the energy change components \hat{G}_I , \hat{G}_{II} and \hat{G}_{ss} calculated behind the crack tip has been found. For a straight crack front, some variation of the mode mixity $\psi(z)$ is found along the crack front. Despite that, a good agreement is found with the averaged mode mixity $\bar{\psi} \approx \hat{\psi}$ obtained based on the energy balance approach behind the crack tip.

Material system covering the range from a compliant glass-fiber composite to a stiff carbon fiber composite has been studied. Thereby, it is with the calculated curves for \hat{G}_{ss} and $\hat{\psi}$ possible to design fatigue test series for extracting the crack growth rate of tunneling cracks in secondary oriented layers addressing a number of different mode-mixity values. Even though the analyses is a linear elastic static analysis, the results can even be used in relation to fatigue studies in a similar way as done in [12]. Tunneling cracks is for fatigue of many authors [6, 7, 13, 16, 21] considered as the initiation fatigue damage mechanism influencing other fatigue damages mechanism later during the fatigue loading.

5.1 On crack face closure

As mentioned, the present linear FE-model does not model crack face contact. Omitting crack face contact - as in the present study - can result in negative normal crack opening displacements (crack face penetration) which is considered unphysical. A more rigorous modelling could include modeling with contact surfaces and friction. But then the modelling would become non-linear (the contact area must be found by iteration) and thus would require longer computation time. Actually modelling the contact may influence the remaining crack opening shape slightly both for the δ_n and δ_t but as this is only the case for smaller layup angles, the effect of this on the crack opening shape will be neglected here.

The precise influence on \hat{G}_{II} will depend on the friction between the crack surfaces given $\hat{G}_{II} = 0$ in case of sticking friction contact at the interface. For a friction-less contact, the (non-physical) crack face penetration is on the other hand only expected to have a minor influence on the \hat{G}_{II} value. ~~which are the one shown in figure 16~~[LAPM: Bent: lets talk about this].

5.2 Thin off-axis plies

The present study (Fig. 13) shows that for very thin off-axis plies (h/H approaching 0), such as backing bundles in non-crimp fabrics, the normalized energy release rate will only be slightly lower similar to what is found in figure 13.

The results of the present paper suggest that the most efficient ways of decreasing the energy release rate is to decrease the thickness of the backing plies, h (see figure 13) and to select low off-axis angles (see figure 18).

5.3 The simplified mode mixity calculation

It is encouraging that there is a good agreement between results obtained by the energy account method from the half-width crack case including a straight crack tip and the full-width crack case without a crack-tip at the front end of the tunneling crack as shown in figure 8. This suggests that the use of the proposed energy accounting approach on a full-width model (avoiding a crack tip) can give both the average energy release rate and the average mode mixity. Then, the finite element model would not need to include the crack tip of the advancing tunneling crack, and this enables a more simpler mesh and thus a much faster analysis of tunneling crack problems. [In addition, this will also open up the possibility of analysing the off-axis tunnel crack as a two dimensional problem. Something which will be investigated in a future study.](#)

6 Conclusions

The energy release rate and the mode mixity has been determined for off-axis orientations covering $\theta \in [0; 90]^\circ$ of a balanced and symmetric $[0/\theta/0/-\theta]_s$ laminate. The results has been determined for structural relevant glass and carbon fiber reinforced composites with a ply stiffness going from 30 GPa for the glass-fiber reinforced lamina to 270 GPa for the carbon fiber reinforced lamina. The analysis has been simplified by replacing a crack-tip stress intensity factor analysis with a off-axis generalization of the Ho and Suo [4] energy accounting approach. The determined energy release rate and the mode mixity factors can be used designing laminates for off-axis crack-growth experiments during static and fatigue loading similar to the experiments performed in [12, 7].

Acknowledgements

References

1. Abaqus: ABAQUS 2019 Theory manual, Online Documentaion Help. Dassault Systmes (2019)
2. Beuth, J.L.: Cracking of thin bonded films in residual tension. *International Journal of Solids and Structures* **29**(13), 1657–1675 (1992). DOI 10.1016/0020-7683(92)90015-L
3. Glud, J.A., Dulieu-Barton, J.M., Thomsen, O.T., Overgaard, L.C.T.: Micro-mechanical multiaxial fatigue model for crack density evolution and stiffness degradation (2015)
4. Ho, S., Suo, Z.: Tunneling cracks in constrained layers. *Journal of Applied Mechanics* **60**, 890–894 (1993)
5. Hutchinson, J., Suo, Z.: Mixed mode cracking in layered materials. *Advances in Applied Mechanics* **29**, 63–191 (1992)
6. Jamison, R., Schulte, K., Reifsnider, K., Stinchcomb, W.: Characterization and Analysis of Damage Mechanisms in Tension-Tension Fatigue of Graphite/Epoxy Laminates pp. 21–21–35 (2008). DOI 10.1520/stp30196s
7. Jespersen, K.M., Glud, J.A., Zangenberg, J., Hosoi, A., Kawada, H., Mikkelsen, L.P.: Uncovering the fatigue damage initiation and progression in uni-directional non-crimp fabric reinforced polyester composite. *Composites Part A: Applied Science and Manufacturing* **109**, 481–497 (2018). DOI 10.1016/j.compositesa.2018.03.002
8. Jespersen, K.M., Mikkelsen, L.P.: Three dimensional fatigue damage evolution in non-crimp glass fibre fabric based composites used for wind turbine blades. *Composites Science and Technology* **153**, 261–272 (2017). DOI 10.1016/j.compscitech.2017.10.004

9. Mandell, J., Samborsky, D., Miller, D.: 7 - effects of resin and reinforcement variations on fatigue resistance of wind turbine blades. In: P. Brøndsted, R.P. Nijssen (eds.) *Advances in Wind Turbine Blade Design and Materials*, Woodhead Publishing Series in Energy, pp. 210 – 250. Woodhead Publishing (2013). DOI <https://doi.org/10.1533/9780857097286.2.210>
10. Mikkelsen, L.P.: The fatigue damage evolution in the load-carrying composite laminates of wind turbine blades. In: A. Vassilopoulos (ed.) *Fatigue life prediction of composites and composite structures*, second edn. Elsevier (2019)
11. Nakamura, T., Kamath, S.M.: Three-dimensional effects in thin film fracture mechanics. *Mechanics of Materials* **13**(1), 67–77 (1992). DOI [10.1016/0167-6636\(92\)90037-E](https://doi.org/10.1016/0167-6636(92)90037-E)
12. Quaresimin, M., Carraro, P., Mikkelsen, L., Lucato, N., Vivian, L., Brøndsted, P., Sørensen, B., Varna, J., Talreja, R.: Damage evolution under cyclic multiaxial stress state: A comparative analysis between glass/epoxy laminates and tubes. *Composites Part B: Engineering* **61**, 282–290 (2014). DOI [10.1016/j.compositesb.2014.01.056](https://doi.org/10.1016/j.compositesb.2014.01.056)
13. Reifsnider, K., Jamison, R.: Fracture of fatigue-loaded composite laminates. *International Journal of Fatigue* **4**(4), 187 – 197 (1982). DOI [https://doi.org/10.1016/0142-1123\(82\)90001-9](https://doi.org/10.1016/0142-1123(82)90001-9)
14. Shih, C.F., Asaro, R.J.: Elastic-Plastic Analysis of Cracks on Bimaterial Interfaces: Part I – Small Scale Yielding. *Journal of Applied Mechanics* (2), 299. DOI [10.1115/1.3173676](https://doi.org/10.1115/1.3173676)
15. Shih, C.F., Moran, B., Nakamura, T.: Energy release rate along a three-dimensional crack front in a thermally stressed body. *International Journal of Fracture* **30**(2), 79–102 (1986). DOI [10.1007/BF00034019](https://doi.org/10.1007/BF00034019)
16. Talreja, R.: Fatigue of Composite Materials: Damage Mechanisms and Fatigue-Life Diagrams. *Proceedings of the Royal Society A: Mathematical, Physical and Engineering Sciences* **378**(1775), 461–475 (1981). DOI [10.1098/rspa.1981.0163](https://doi.org/10.1098/rspa.1981.0163)
17. Tong, J.: Three Stages of Fatigue Crack Growth in GFRP Composite Laminates. *Journal of Engineering Materials and Technology* **123**(1), 139–143 (2000). DOI [10.1115/1.1286234](https://doi.org/10.1115/1.1286234)
18. Tong, J., Guild, F., Ogin, S., Smith, P.: On matrix crack growth in quasi-isotropic laminates. experimental investigation. *Composites Science and Technology* **57**(11), 1527 – 1535 (1997). DOI [https://doi.org/10.1016/S0266-3538\(97\)00080-8](https://doi.org/10.1016/S0266-3538(97)00080-8)
19. Vallons, Katleen, Adolphs, Georg, Lucas, Paul, Lomov, Stepan V., Verpoest, Ignaas: Quasi-ud glass fibre ncf composites for wind energy applications: a review of requirements and existing fatigue data for blade materials. *Mechanics & Industry* **14**(3), 175–189 (2013). DOI [10.1051/meca/2013045](https://doi.org/10.1051/meca/2013045)
20. Wang, Y., Mikkelsen, L.P., Pyka, G., Withers, P.: Time-Lapse Helical X-ray Computed Tomography (CT) Study of Tensile Fatigue Damage Formation in Composites for Wind Turbine Blades. *Materials* **11**, 2340 (2018). DOI [10.3390/ma11112340](https://doi.org/10.3390/ma11112340)
21. Zangenberg, J., Brøndsted, P., Gillespie, J.W.: Fatigue damage propagation in unidirectional glass fibre reinforced composites made of a non-crimp fabric. *Journal of Composite Materials* **48**, 2711–2727 (2013). DOI [10.1177/0021998313502062](https://doi.org/10.1177/0021998313502062)